PCCP

Accepted Manuscript

ROYAL SOCIETY OF CHEMISTRY

www.rsc.org/pccp

Article type: Full Paper

Enhancing Photo-induced Ultrafast Charge Transfer across Heterojunctions of CdS and Laser-Sintered TiO_2 Nanocrystals

Bryan T. Spann,[†,a] S. Venkataprasad Bhat,[†,a] Qiong Nian,[b] Kelly M. Rickey,[a] Gary J. Cheng,[b] Xiulin Ruan,[a,] and Xianfan Xu[a,*]*

Abstract

Enhancing the charge transfer process in nanocrystal sensitized solar cells is vital for the improvement of their performance. In this work we show a means of increasing photo-induced ultrafast charge transfer in successive ionic layer adsorption and reaction (SILAR) CdS–TiO_2 nanocrystal heterojunctions using pulsed laser sintering of TiO_2 nanocrystals. The enhanced charge transfer was attributed to both morphological and phase transformations. At sufficiently high laser fluencies, volumetrically larger porous networks of the metal oxide were obtained, thus increasing the density of electron accepting states. Laser sintering also resulted in varying degrees of anatase to rutile phase transformation of the TiO_2, producing thermodynamically more favorable conditions for charge transfer by increasing the change in free energy between the CdS donor and TiO_2 acceptor states. Finally, we report aspects of apparent hot electron transfer as a result of the SILAR process which allows CdS to be directly adsorbed to the TiO_2 surface.

Keywords: nanocrystals, solar cells, charge transfer, transient absorption, laser sintering

1. Introduction

Nanocrystal sensitized solar cells (NCSCs) have been under extensive investigation due to their potentially high photo-conversion efficiencies and reduced cost.[1–8] Various strategies have been employed to maximize NCSC device efficiencies, however, the current record efficiencies remain around ~ 5.4%, which is significantly lower than the predicted limit of ~ 20%.[9,10] To create NCSCs, two prominent techniques have arisen: the first relies on the fine tuning of the nanocrystal sensitizer size to control the band-gap energy using colloidal chemistry techniques,[11–17] the second is via successive ionic layer adsorption and reaction (SILAR).[18–23] Within these two approaches, emphasis has been brought upon nanocrystal – metal oxide (NC–MO) heterojunction in order to better understand the physical underpinnings of the charge transfer process.[2,3,13,15,19,24]

In this report we examine the electron transfer process between SILAR CdS–TiO_2 heterojunctions, and propose a means of enhancing ultrafast charge transfer using laser processing to modify the morphology and crystalline phase of the MO. We focus on SILAR heterojunctions because, unlike colloidal synthesis of nanocrystals, it does not require the use of surface-attached organic ligands. Organic ligands have been found in several reports to act as relaxation and transfer pathways for excitons.[25–27] The quenching of excitons through organic ligands in NCSCs is detrimental to overall device performance.[15] Furthermore, the ultrafast charge transfer between NC and MO determined from the ultrafast measurement is ambiguous when ligands are present, because it is difficult to discern whether electrons are transferring to the desired MO, to the various organic ligands attached to the surface, or relaxing through other non-radiative phenomenon such as to surface trap states or Auger-thermalization.[26,28–30] On the other hand, when SILAR is used, ultrafast charge transfer can be more easily understood due to the absence of ligands. The presence of organic ligands also creates an additional dielectric barrier of which electrons must overcome in order to transfer

to the MO.[15,17] Tisdale and Zhu pointed out that the thickness of the dielectric barrier would dictate the potential for hot-electron and band-edge charge transfer. Shorter distances between NCs and MO would enhance electronic coupling for hot-electron charge transfer.[17] For SILAR heterojunctions the resistive dielectric layer is not present, thus providing more favorable interfacial conditions for the hot-electron transfer process. Various research groups have shown evidence for hot-electron transfer, e.g., Tisdale and Zhu reported hot-electron transfer in monolayer PbSe QDs coupled to TiO_2,[16] Sambut et al. and more recently Yang et al. have reported electron transfer occurring within 50 fs[31] and 6.4 fs[32] between PbS NCs and TiO_2, each of these studies had the ligand dielectric barrier. However, others have found much longer timescales for electron injection that suggest hot-electron transfer is not occurring, for example the work by Pijpers et al.[33] and Cánovas et al.,[34] both of which have used THz time domain spectroscopy for their conclusions. Despite, the studies by Pijpers et al.[33] and Cánovas et al.,[34] we expect the SILAR heterojunctions could have a greater probability of transferring hot-electrons as a result of the closer proximity of NC and MO due to the lack of the ligand barrier.

A drawback to NC sensitized solar cells is reduced electron mobility once the exciton has disassociated into individual electrons and holes. This is a result of constricted electron transfer pathways between neighboring MO NCs. While investigations into enhanced charge transfer by tuning, *e.g.*, the NC size and shape,[12,13] and metal oxide chemical composition,[15,19] fewer works have been done to observe the effects of morphological dependence of the MO,[35] and none have studied the effects of the transformation of MO crystalline phase on ultrafast charge transfer. In order to facilitate enhanced electron mobility, we employ pulsed laser sintering to induce a mesoporous to macroporous structural transformation in the MO NCs. Accompanied with the morphological transformation is an anatase to rutile phase transformation which enhances electron transfer from SILAR adsorbed CdS NCs to the TiO_2 MO. In addition to enhanced electron transfer rates, we also show evidence suggesting hot-

electron transfer between CdS and TiO_2, as a result of this phase/morphology transformation as well as the close proximity of NC and MO due to the lack of organic ligands.

2. Experimental Details

Sample fabrication: To prepare the CdS–TiO_2 SILAR samples, Degussa P25 mixed phase (80% anatase and 20% rutile) TiO_2 NCs were used for the MO electron acceptor. The TiO_2 NCs were roughly spherical with diameters on the order of 10-20 nm. The TiO_2 films were deposited on a glass substrate using the doctor blade technique[15] and were found to be approximately 3.5 μm thick (measured via cross-sectional SEM). All TiO_2 films were calcined at 450°C for one hour. A pulsed KrF (248 nm wavelength) excimer laser with a repetition rate of 10 Hz and pulse duration of 25 ns was used to sinter the TiO_2 films with fluences ranging from 50 to 200 mJ/cm^2. The sintering was performed in a 20 mtorr vacuum environment to minimize sintering induced surface defects in the TiO_2. The TiO_2 NC films were each exposed to the excimer laser for 1 second. After laser irradiation, CdS was adsorbed on the TiO_2 films using the SILAR technique, which involves dipping the TiO_2 films into 0.1 M $Cd(ClO_4)_2$, followed by a dipping into 0.1 M Na_2S aqueous solutions at room temperature in an inert environment.[21] Following this, the samples were rinsed with distilled water. For all CdS–TiO_2 samples we repeated this dip-dip-rinse cycle 8 times to ensure full coverage and adequate growth of the CdS nanocrystals.

Structural and surface characterization: The TiO_2 films were imaged via scanning electron microscopy (SEM, Hitachi S-4800). The crystalline phase of the TiO_2 was determined by means of Raman microscopy (Horiba LabRAM HR). After the CdS was adsorbed to the surface of the TiO_2, energy dispersive X-ray spectroscopy (EDX, FEI Philips XL-40 SEM) was used to compare the ratio of Cd to Ti for each sample. After all optical spectroscopy was performed, transmission electron microscopy (TEM, Titan 80-300 kV) was

used to image the CdS - TiO_2 interface conditions and verify crystalline phase. TEM samples were prepared by dispersing the powder scratched from the prepared films in ethanol and placing droplets of the suspension on carbon coated copper TEM grids.

Linear and nonlinear optical characterization: For the linear absorption spectroscopy, a Perkin Elmer Lambda 950 UV/Vis/NIR spectrophotometer was used. The transient absorption spectroscopy (TAS) experiment employs a traditional non-collinear pump-probe scheme consisting of a Spectra Physics femtosecond pulsed laser amplifier that produces 70 fs pulses at a central wavelength of 800 nm and a repetition rate of 5 kHz. The probe leg is sent into a Quantronix TOPAS optical parametric amplifier (OPA). The probe wavelength from the OPA was set to 490 nm (tuned to the conduction band-edge of CdS NC). The pump beam is sent through a mechanical chopper rotating at a frequency of 500 Hz, then through a second harmonic crystal to generate 400 nm pulses for sample excitation. The pump and probe are then focused on the sample non-collinearly to $1/e^2$ spot diameters of 320 μm and 150 μm for pump and probe, respectively. The pump fluence was set to approximately 80 $\mu J/cm^2$ to ensure the absence of multi-particle Auger recombination.[14] We placed a 450 nm long-pass light filter after the sample to eliminate the scattered pump photons from reaching our detector. In order to help eliminate laser noise, we used a balanced photo-detector for probe and reference beam detection. Additionally, two 10 nm full width half max (FWHM) band-pass filters centered at the 490 nm probe wavelength were used for each side of the balanced photo-detector. The 10 nm band-pass filters provide a spectrally integrated signal to cover the variance in bandedge energy as a result of the size dispersion of the CdS NCs.

3. Results and Discussion

3.1. TiO_2 Characterization

The effects of pulsed laser sintering are immediately obvious in surface SEM images of the TiO_2 films. A representative TiO_2 film at a 50 μm scale is shown in Figure 1A, revealing variable coverage as a result of the doctor blade technique. Figure 1B – F show the change in morphology as a result of sintering on the TiO_2 NC films, with B and F representing the two extremes, no sintering (0 mJ/cm^2) and the higher laser fluence used, 200 mJ/cm^2, respectively. Growth in fused TiO_2 features appear roughly as 100 nm, 1 μm, 5 μm, and 10 μm for the laser fluences of 50, 100, 150, and 200 mJ/cm^2, respectively. Furthermore, relatively larger scale networks appear to be forming for sintering cases 100 mJ/cm^2 and above, while the 50 mJ/cm^2 sample shows only highly localized sintered TiO_2 networks. The larger networks of sintered TiO_2 are expected to enhance mobility of electrons once they have transferred into the TiO_2. Furthermore, the density of accepting states is also expected to increase as will be discussed later. All samples, except the 200 mJ/cm^2 sample, show visible porosity in their SEM images.

Raman spectra were collected for the TiO_2 sintered films and are shown in Figure 2. The anatase (ana) and rutile (rut) phase peaks are labeled with dashed vertical lines. The dominant anatase peaks are assigned to the following modes: E_g^{ana} (~ 150 cm^{-1} and 640 cm^{-1}), B_{1g}^{ana} (~ 400 cm^{-1} and 515 cm^{-1}), and A_{2g}^{ana} (515 cm^{-1}).[36] The rutile phase peaks are assigned to the following modes: E_g^{rut} (~ 446 cm^{-1}) and A_{1g}^{rut} (~ 610 cm^{-1}).[37] The Raman data show that as the sintering fluence is increased, the TiO_2 films undergo varying degrees of phase transformation from anatase to rutile. This is evident by viewing the Raman spectra of un-sintered sample (0 mJ/cm^2 fluence), which shows predominantly anatase phase Raman modes (also expected from the well-known Degussa P25 TiO_2). As the sintering fluence increases, growth in the E_g^{rut} and A_{1g}^{rut} modes and decay in the anatase modes is very clear. Furthermore,

once the sintering fluence reaches 150 mJ/cm^2, the rutile phase begins to dominate the Raman spectra with smaller contributions from the anatase phase peaks. At 200 mJ/cm^2, the Raman spectra display only a low intensity E_g^{ana} peak, suggesting almost a full phase transformation. The broad peak centered at 240 cm^{-1} is attributed to a second-order rutile phonon mode.[38]

3.2. CdS-TiO_2 Adsorption Characterization

Using the SILAR technique, described in the sample preparation section below, CdS was adsorbed to the surface of the unsintered and sintered TiO_2 samples. Linear absorption (an approximately 1 cm^2 sampling area was used to average out the variable coverage of films) and energy-dispersive X-ray spectroscopy (EDX) showed that the relative amount of Cd to Ti were consistent for all samples as shown in Figure 3A and B, respectively. Figure 3A also shows the linear absorption data of a CdS–SiO_2 sample that was used in this study as a reference for both linear absorption measurements and more importantly for transient absorption measurements. The offset of the CdS–TiO_2 samples is a result of light scattering from the TiO_2 surface, which increases for longer wavelengths under higher sintering conditions. The EDX data presented in Figure 3B show the relative amount of Cd to Ti for each sample. The similar adsorption percentages indicate that sintering does not deteriorate the adsorption capability. It also allows us to directly compare the charge transfer in each sample on an equal basis.

Transmission electron microscopy (TEM) was used to observe the nanoscale interfacial conditions that exist between the CdS and TiO_2. Figure 4 shows both the low resolution and high resolution images obtained for samples with unsintered and sintered TiO_2 particles (150 mJ/cm^2 sintering fluence). The growth of TiO_2 particles upon laser sintering is shown by the relatively larger size of the sintered particles in Figure 4B when compared with the unsintered particles in Figure 4A. A high resolution TEM image of the unsintered sample

is shown in Figure 4C, with the crystal planes noted for both the anatase and rutile phases of TiO_2. We identify the (001) and (101) planes of anatase TiO_2 with interplanar spacing's of d = 0.235 and 0.355 nm, respectively. Figure 4D shows the high resolution TEM image of the 150 mJ/cm^2 sintered case and we are able to identify the (110) plane of rutile phase TiO_2 with an interplanar spacing of d = 0.325 nm. For Figures 4C and D we mark the (100) CdS planes with d = 0.356 nm. Figure 4D (the sintered sample) had only rutile phase crystal planes indicating the phase transformation of TiO_2. Furthermore, the interfacial condition between the sintered TiO_2 particles of bigger size also appears to show larger surface area through which electron could transfer from CdS to the TiO_2.

3.3. Transient Absorption

Transient absorption spectroscopy (TAS) measurements were performed using a pump wavelength of 400 nm (3.1 eV) and a probe wavelength tuned to the conduction band-edge of the CdS NCs at 490 nm (2.53 eV); see Figure 3A. The conduction band-edge of the CdS was determined by first probing at 500 nm with 10 nm band-pass filters and all samples' TAS signals exhibited photo-induced absorption features which suggests below band-edge probing. The probe wavelength was then decreased to 490 nm with 10 nm band-pass filters and all samples' TAS signals showed no photo-induced absorption, suggesting the probe photons are directly probing the average band-edge energy (we have demonstrated this in our earlier works, see refs. [29,30] for more details). By probing at the conduction band-edge we are able to directly monitor the population of this electronic level, therefore, the depopulation of this level corresponds to electron transfer or recombination with hole. In order to estimate the charge transfer rate from the TAS signals, we employ a similar strategy to other works and use a reference sample with SiO_2 in place of TiO_2.[15,19,39] The TAS signal from the CdS–SiO_2 sample will provide purely CdS exciton relaxation; *i.e.*, without charge transfer because of the insulator nature of SiO_2 (9.2 eV band-gap energy).[15]

TAS data of CdS-SiO_2 superposes several photo-physical phenomena, namely once the pump photons arrive at the sample, an exciton is generated and because the probe beam is tuned to the conduction band-edge of the CdS, this energy state is already occupied; this leads an increase in transmission. This effect is caused by state-filling induced bleach.[40] Another consequence of this is an increase in stimulated emission and spontaneous emission which also gives rise to increased transmission.[25] As the probe pulse is delayed with respect to the pump pulse, electrons and holes begin to relax non-radiatively to lower energy surface-trap-states, followed by radiative recombination of electrons and holes.[23] For the samples with CdS adsorbed to TiO_2, the same exciton relaxation mechanisms are active in the CdS. However, an additional electron relaxation pathway arises via transfer to the TiO_2. This allows us to quantitatively analyze the TAS relaxation data by considering the difference in relaxation rate between the CdS TiO_2 sample and the CdS-SiO_2 reference sample. The electron transfer rate (k_{ET}) between CdS and TiO_2, which may be calculated as,[19,39]

$$k_{ET} = \frac{1}{(\tau)_{CdS-TiO_2}} - \frac{1}{(\tau)_{CdS-SiO_2}} \quad (1)$$

where $(\tau)_{CdS-TiO_2}$ and $(\tau)_{CdS-SiO_2}$ are the relaxation times for the CdS–TiO_2 sample and the CdS–SiO_2 reference sample, respectively. The results of the TAS absorption data are presented in Figure 5, with the inset showing the first 40 ps of the decay. In order to account for the variable coverage in the films (*e.g.*, see Figure 1A) we used relatively large pump and probe spot sizes of 320 μm and 150 μm, respectively. Furthermore, the TAS results presented in Figure 5 represent the average of five measurements on each sample. The error-bars included on each line represent the standard deviation between five different spatial locations on the sample. From Figure 5, the CdS–SiO_2 sample shows the slowest relaxation (due to absence of charge transfer). Furthermore, a background photoluminescence (PL) is present for this sample, shown by the non-zero baseline in the TAS signal. We have eliminated the possibility of this signal being a result of scattered pump and probe photons by using light filtration

described in the Experimental Details Section. The PL background of the CdS–SiO_2 is likely to be present based on relaxation of the electrons into long-lived surface traps states that exist due to deficiently passivated surfaces and the dangling bonds that are present. Additionally, we believe that a photocharging effect could be present which can also lead to long lived PL features.[41] The background PL signal contributes to the entire time signal, therefore, for the analysis of charge transfer, the background signal is subtracted and the signal is re-normalized for the charge transfer calculations.

For the CdS–TiO_2 samples, significant charge transfer is evident for all samples (shown by faster exponential decay in Figure 5). Furthermore, the PL background has been predominantly quenched for all CdS–TiO_2 samples, which is indicative of band-edge charge transfer.[19] Figure 5 also shows the sintering effects on the TAS; as the sintering laser fluence increases, the charge transfer increases up to the laser fluence of 150 mJ/cm^2. Using the laser fluence of 200 mJ/cm^2, the transfer reduces relative to the 150 mJ/cm^2, close to that sintered using the laser fluence of 100 mJ/cm^2.

Biexponential fits of the TAS data were used to quantify the fast and slow components of relaxation. For the CdS-SiO_2 sample the fast component corresponds to relaxation of excitons into surface trap states and the slow component corresponds to radiative recombination, these two processes define the intrinsic decay of the CdS.[19,39] For the CdS-TiO_2 samples, the same fast and slow processes exist with the addition of the charge transfer pathway to the TiO_2.[19,39] We have considered both fast and slow processes separately in our analysis, by segregating the components of the biexponential fits of the normalized TAS data:

$$\Delta T / T_o = C_1 e^{-t/\tau_1} + C_2 e^{-t/\tau_2} \quad (2)$$

Where, C_i are the pre-exponential factors which correspond to the relative amplitude of each lifetime, and τ_i are the decay times associated with each term.[19,39] We define the first term of the biexponential fit ($C_1 e^{-t/\tau_1}$) to represent the fast component, the second term ($C_2 e^{-t/\tau_2}$)

represents the slow component. From equation (2) we can define two new equations in the form of equation (1) to calculate the electron transfer rates that occur during the fast and slow timescales separately, those are:

$$k_{F,ET} = (1/\tau_1)_{CdS-TiO_2} - (1/\tau_1)_{CdS-SiO_2}$$
$$k_{S,ET} = (1/\tau_2)_{CdS-TiO_2} - (1/\tau_2)_{CdS-SiO_2} \quad (3)$$

Where the subscripts *F,ET* and *S,ET* denote the electron transfer during the fast and slow timescales, respectively. Note: here we are not suggesting that there are fast and slow electron transfer processes, rather we are using the two terms to portray the relative amount of electrons transfering during the two different timescale in this measurement. We have employed this method to better portray the relative contributions of charge transfer over the two timescales. The biexponential fitting parameters and electron transfer rate calculation results are shown in Table 1. We can see from Table 1 that the slow radiative recombination component (i.e., C_2) is the dominant physical event for the CdS-SiO_2 sample, whereas for the CdS-TiO_2 samples, the contribution of the fast component in the decay (i.e., C_1) is more dominant when compared with the intrinsic decay of the CdS-SiO_2 sample. In order to depict the results more clearly, the results of the electron transfer rate (k_{ET}) calculations are presented in Figure 6. Again, in Figure 6, the laser sintering fluence of 150 mJ/cm^2 yields the highest charge transfer rate for both fast and slow components of the electron transfer process. In fact, when comparing it to no-sintering, there is approximately a two-fold increase in the rate of transfer for both fast and slow process. This two-fold increase in electron charge transfer is significant because hole transfer from QDs has been shown to be on the order of ~4 ps for InP QDs coupled with a tetramethyl-p-phenylenediamine hole acceptor, making both electron and hole transfer enhancement crucial to the overall device performance.[42] We have also calculated an average electron charge transfer rate using the following expression[19,39]:

$$\langle k_{ET} \rangle = 1/\langle \tau \rangle_{CdS-TiO_2} - 1/\langle \tau \rangle_{CdS-SiO_2} \quad (4)$$

where the weighted average relaxation times can be calculated as:[19,39]

$$\langle \tau \rangle = \frac{\sum_{i=1}^{n} C_i \tau_i^2}{\sum_{i=1}^{n} C_i \tau_i} = \frac{C_1 \tau_1^2 + C_2 \tau_2^2}{C_1 \tau_1 + C_2 \tau_2} \quad (5)$$

Where the C_i and τ_i come from the biexponential fit function. The weighted average electron transfer rate is often used,[19,39,43] but here we show that some insight is lost when only this value is reported. For instance, the results of the $\langle k_{ET} \rangle$ calculation are found in Table 1 and show that the electron transfer rate is dominated by the slower component of the relaxation. However, as evident from Table 1, Figure 5, and Figure 6, both timescales show varience in the charge transfer rate.

3.4. Insights from Marcus Theory

In order to understand the mechanisms leading to increased electron transfer, we must consider the energy band alignments for each of the materials in the charge transfer process. Shown in the inset of Figure 6 is the vacuum energy level containing the relative energy level differences in the conduction band minimum (CBM) and valence band maximum (VBM) for the constituent materials. As shown in the Raman spectroscopy results (Figure 2) and also the TEM results (Figure 4), the relative amount of rutile phase to anatase phase in the TiO_2 is increased as the sintering fluence is increased. The rutile phase CBM is approximately 0.2 eV lower than the anatase phase CBM,[37,44] thus an increasing electronic potential between donor and accepting states exists between the CdS and TiO_2 as the sintering increases. This acts as a stronger driving force for electrons to be transferred. Furthermore, it has been shown that by introducing an intermediate level anatase TiO_2 structure, once electrons are transfer to the rutile TiO_2 it reduces the potential for recombination.[37]

The fundamental reasons for the increase in charge transfer can be clarified further using Marcus theory. To elucidate the details of charge transfer in NC – MO systems, various

groups have successfully applied the many-state non-adiabatic Marcus model.[15,17,35,45] Using Marcus theory, the electron transfer rate between donor and acceptor states can be calculated as,[15]

$$k_{ET} = \frac{2\pi}{\hbar}\int_{-\infty}^{\infty} \rho(E)\left|\bar{H}(E)\right|^2 \frac{1}{\sqrt{4\pi\lambda k_B T}} \exp\left(-\frac{(\lambda + \Delta G + E)^2}{4\lambda k_B T}\right) dE \quad (4)$$

where $\rho(E)$ is the energy dependent density of accepting states (DOS) in the MO. $\bar{H}(E)$ is an overlap matrix element, λ is the system reorganizational energy, k_B is Boltzmann's constant, $\hbar$ is Planck's constant, T is the temperature, and ΔG is the change in system free energy. Although all terms in equation (3) affect the charge transfer rate, for this study $\rho(E)$ and ΔG dominate the difference in charge transfer as a result of the altered phase MO. The wavefunction overlap matrix element $\bar{H}(E)$ is typically assumed to be independent of energy and the reorganizational energy λ is expected to be independent of the MO and depend only on the CdS sensitizer.[15,17,35,45] To establish the sources of the increase in charge transfer, we first consider the DOS. In bulk-like MOs, assuming a parabolic dispersion, $\rho(E)$ can be described by:[15]

$$\rho(E) = V_0 \frac{(2m_e^*)^{3/2}}{2\pi\hbar^3}\sqrt{E} \quad (5)$$

where V_0 is the localized electron acceptor volume of the crystal. We expect V_0 to not vary between sintering conditions becuase the interfacial conditions between donor and acceptor are similar. The m_e^* variable is the effective mass of the electrons in TiO_2. For higher sintering conditions, we expect an increase in $\rho(E)$ for the TiO_2 because of the increase in electron effective mass, $m_e^* \sim 1m_0$ and $m_e^* \sim 8-20m_0$ for anatase and rutile, respectively.[46] The increased DOS in the MO results higher potential for electron transfer. The other dominant modification, as a result of the phase transformation, is the change in free energy

ΔG . Tvrdy *et al.* derived a simple expression to calculate the change in free energy for NC – MO systems,[15]

$$\Delta G \approx E_{MO} - E_{1Se} + (1+C)\frac{e^2}{\varepsilon_{QD} R_{QD}} + \frac{e^2}{2R_{QD}}\left(1+\frac{C}{\varepsilon_{QD}}\right) - \frac{e^2}{4(R_{QD}+h)}\frac{\varepsilon_{MO}-1}{\varepsilon_{MO}+1} \qquad (6)$$

where E_{MO} and E_{1Se} are the electron energies at the CBM of the TiO_2 and CdS, respectively, e is the fundamental charge constant, R_{QD} is the average radius of the CdS NCs, h is the spatial separation between donor and acceptor, ε_{QD} and ε_{MO} are the dielectric permittivity of the CdS and TiO_2, respectively, and finally $C \approx 0.786$ is a numerical integration constant.[15] As mentioned previously, the anatase to rutile phase conversion results in a 0.2 eV reduction in E_{MO}, resulting in CBM values of -4.41 eV and -4.61 eV, respectively.[37,44] The dielectric permittivity of the TiO_2 are $\varepsilon_{MO} \approx 9.9$[15] and 6.33[46] for anatase and rutile, respectively. Both changes result in modifications to ΔG .

Taking only the energy dependent parameters and considering the cases of pure anatase and rutile phases, we can use the experimentally obtained parameters R_{QD} (~7 nm) and E_{1Se} (~ -3.7 eV)[47] and values from literature discussed above to calculate a relative increase in band-edge charge transfer as a result of the difference in ΔG , *i.e.*,

$$\frac{k_{ET,Rut}}{k_{ET,Ana}} \propto \left(\frac{m^*_{e,Rut}}{m^*_{e,Ana}}\right)^{3/2} \frac{\int_{-\infty}^{\infty} \sqrt{E}\exp\left(-\frac{(\lambda+\Delta G_{Rut}+E)^2}{4\lambda k_B T}\right)dE}{\int_{-\infty}^{\infty} \sqrt{E}\exp\left(-\frac{(\lambda+\Delta G_{Ana}+E)^2}{4\lambda k_B T}\right)dE} \qquad (7)$$

Using equation (6), we find that $\Delta G_{Ana} = -0.546\,\text{eV}$ and $\Delta G_{Rut} = -0.748\,\text{eV}$. Using these values for equation (7) with λ = 10 meV,[17] we find that $\frac{k_{ET,Rut}}{k_{ET,Ana}} \approx 26.59$ to105.1, indicating a large increase in theoretical charge transfer rate as a result of the change in free energy and the change in effective mass between the two phases. The effective mass contributions provide the large varience in the ratio as result of $m_e^* \sim 8-20m_0$ for the rutile TiO_2.

The eventual reversal of charge transfer increase when the sintering laser fluence surpasses 150 mJ/cm^2 could be explained by an unfavorable decrease in TiO_2 adsorption surface area. For the 200 mJ/cm^2 fluence, the microporous structure appears to be lost (see Figure 1 (F)), suggesting that the CdS would have less surface area to adsorb to. Furthermore, because the EDX data shows very similar Cd:Ti quantity levels, the CdS could be adsorbed to other CdS and not to the TiO_2 (and this appears to be the case according to Figure 4B, showing the smaller CdS NCs stacked on one another), this would result in a reduction in charge transfer.

3.5. Aspects of Hot Electron Transfer

In addition to the band-edge charge transfer, we also analyze the TAS signal rise times. The rise time of the TAS signals correspond to the hot-exciton relaxation time in the CdS NCs. The TAS data are presented in Figure 7A with the corresponding rise time values presented in Figure 7B. Note that for Figure 7A the background long-lived surface trap photoluminescence (STPL) has been subtracted out from the CdS-SiO_2 signal to provide a direct comparison between rise times. This signal is likely a result of long-lived deep trap emission or potentially photo-charging from resulting from prolonged UV exposure as mentioned previously, however this subtraction will not modify the rise time analysis. From Figure 7B it is evident that there is a considerable difference in rise times when comparing the various sintering fluences. It is evident that the 0 and 50 mJ/cm^2 samples have similar rise times of approximately 480 fs, while the 100 and 150 mJ/cm^2 cases show an increase in rise time to roughly 750 to 780 fs. The increase in TAS rise time could potentially be explained as a lack of hot-electron transfer from the CdS to TiO_2. To analyze this issue, consider the inset of Figure 7A, the rise time of the signal denotes the time for electrons high in the conduction band of the CdS to relax down to the band-edge, this is the intraband relaxation rate (k_{IB}). If

all of the electrons are allowed to relax to the CBM of the CdS, this would correspond to the longest possible saturation time, i.e. the intrinsic rise time of the CdS. As we can see from Figure 7B, the intrinsic rise time of the CdS-SiO_2 is nearly 900 fs, which is the longest rise time of all of the samples tested. Furthermore, as mentioned above, we employed a low pump fluence of 80 μJ/cm^2, therefore, we can neglect the Auger-recombination.[14] This suggests that a decrease in rise time corresponds to transferring of a small portion of the hot-electron population prior to reaching the band-edge (shown by the k_{Hot} pathway in the inset of Figure 7A), thus causing the band-edge to saturate faster. Based on this argument, the unsintered and the 50 mJ/cm^2 samples show the most hot-electron transfer. For this to be true a key assumption is that the same number of CdS NC must be excited for all cases. Because the linear absorption spectra for the samples all exhibit nearly identical trends and the EDX data show similar amounts of Cd to Ti ratios for all samples, it is likely this assumption is valid. An important observation pertaining to this assumption is that because the linear absorption and Cd:Ti ratios remain constant this requires buildup of CdS on CdS for higher sintering conditions as a result of the reduction in TiO_2 adsorption area. The build up of CdS is evident in Figure 4B, showing CdS not directly adsorbed to the TiO_2 crystallite. Based on this argument, it is fair to assume that if some of the electron population is transferred to the TiO_2 prior to thermalization, this would show up as a reduction in overall population in the TAS measurement, and thus a reduction in overall TAS signal from the band-edge. Based on our measurements, the signal reduction is within the error-bars of the experiment. Therefore, we can conclude that if there is hot-electron transfer occurring, it only contributes almost negligibly to the overall TAS signal. Considering this observation, we would also like to point out that changes in rise time of the TAS signal could also be the result of inter-particle coupling between the CdS NCs which is expected to change based on the TiO_2 morphology.

Inter-particle coupling between CdSe NCs has been demonstrated to have an effect on the intraband relaxation, see for example, the work by Yang et al.[48] and Gao et al.[49]

We believe the apparent hot-electron transfer can be explained via the synthesis process of SILAR. Tisdale and Zhu showed that by considering the radial probability density distribution for a NC, the 2S electron probability density distribution extends substantially farther outside the NC surface than the lower energy 1S probability density distribution.[17] Therefore, hot-electrons have longer range interaction when compared to thermalized electrons. SILAR, as mentioned above, is a direct adsorption technique that is absent of organic ligands, which allows the CdS to be directly attached to the TiO_2 (see TEM images in Figure 4). Common organic ligands and molecular linkers used such as dodecylamine and 2-mercaptopropionic acid (2-MPA) have linker lengths on the order of 0.53 nm.[35] The radial probability distribution is exponentially reduced at distances greater than approximately 0.2 nm outside the donor NC, thus the direct electronic interaction between donor and acceptor for the case of an addition dielectric layer is also drastically reduced.[17] This could explain why we observe hot-electron transfer while Tvrdy *et al.*[15] did not detect such phenomenon. Furthermore, we believe that this proximity argument can be applied to explain why we observe differences in rise times between our samples. For example, by sintering the TiO_2, we effectively reduce the adsorption surface area for the SILAR process, this means that the unsintered sample has the most adsorption surface area, thus more CdS can be directly attached to TiO_2, whereas, the sintered samples have less adsorption area and the CdS can adsorb on other CdS which would eliminate the possibility of hot electron transfer for the spatially separated CdS.

4. Conclusion

To conclude, we used pulsed laser sintering of TiO_2 nanocrystals to enhance charge transfer between CdS and TiO_2. The enhancement in charge transfer is found to be due to the phase transformation induced by the sintering process which increases the relative amount of rutile phase to anatase phase in the TiO_2. This phase transformation increases the electronic potential between donor and accepting states in a thermodynamically favorable way, by increasing the TiO_2 DOS ($\rho(E)$) and reducing the change in free energy (ΔG), thus increasing the charge transfer from the CdS to TiO_2. In addition, we found potential hot-electron transfer for the unsintered sample and the 50 mJ/cm^2 laser sintered sample which was inferred based on TAS signal rise time arguments. The hot-electron transfer is believed to be a result of the direct adsorption of the CdS to the TiO_2 which allows for better electronic interaction between the two materials. For the band-edge electron transfer, it is shown that the 150 mJ/cm^2 laser sintered sample provided the best overall performance in terms of charge transfer. Our findings suggest that optimal sintering conditions could be used to maximize both hot-electron transfer and band-edge electron transfer from CdS to TiO_2.

Acknowledgements

Support for this work was provided by the National Science Foundation and is gratefully acknowledged. The authors wish to thank Dr. Sergey Suslov for assistance with TEM imaging, James Mitchell for assistance with SEM imaging, and Yan Wang for discussions on the charge transfer calculations.

Notes and References

† *These authors contributed equally to this work.*
[a] *Birck Nanotechnology Center and School of Mechanical Engineering, Purdue University, 1205 West State St., West Lafayette, Indiana 47907, United States.*
[b] *School of Industrial Engineering, Purdue University, 315 N. Grant St., West Lafayette, Indiana 47907, United States.*
* *Email: xxu@purdue.edu, ruan@purdue.edu.*

1. M. Grätzel, *Nature*, 2001, **414**, 338–344.

2. P. Kamat, *J. Phys. Chem. Lett.*, 2013, **4**, 908–918.

3. P. V. Kamat, *J. Phys. Chem. C*, 2007, **111**, 2834–2860.

4. A. Nozik, *Phys. E Low-dimensional Syst. Nanostructures*, 2002, **14**, 115–120.

5. H. Zhu and T. Lian, *Energy Environ. Sci.*, 2012, **5**, 9406–9418.

6. C. A. Nelson, N. R. Monahan, and X.-Y. Zhu, *Energy Environ. Sci.*, 2013, **6**, 3508.

7. M. C. Beard, *J. Phys. Chem. Lett.*, 2008, **2**, 1282–1288.

8. G. Conibeer, I. Perez-Wurfl, X. Hao, D. Di, and D. Lin, *Nanoscale Res. Lett.*, 2012, **7**, 193–199.

9. P. K. Santra and P. V Kamat, *J. Am. Chem. Soc.*, 2012, **134**, 2508–11.

10. S. Rühle, M. Shalom, and A. Zaban, *Chemphyschem*, 2010, **11**, 2290–304.

11. K. Zídek, K. Zheng, M. Abdellah, N. Lenngren, P. Chábera, and T. Pullerits, *Nano Lett.*, 2012, **12**, 6393–9.

12. I. Robel, M. Kuno, and P. V Kamat, *J. Am. Chem. Soc.*, 2007, **129**, 4136–7.

13. D. R. Pernik and K. Tvrdy, *J. Phys. Chem. C*, 2011, **115**, 13511–13519.

14. I. Robel, V. Subramanian, M. Kuno, and P. V. Kamat, *J. Am. Chem. Soc.*, 2006, **128**, 2385–2393.

15. K. Tvrdy, P. A. Frantsuzov, and P. V Kamat, *Proc. Natl. Acad. Sci. U. S. A.*, 2011, **108**, 29–34.

16. W. A. Tisdale, K. J. Williams, B. a Timp, D. J. Norris, E. S. Aydil, and X.-Y. Zhu, *Science*, 2010, **328**, 1543–7.

17. W. A. Tisdale and X.-Y. Zhu, *Proc. Natl. Acad. Sci. U. S. A.*, 2011, **108**, 965–70.

18. C.-H. Chang and Y.-L. Lee, *Appl. Phys. Lett.*, 2007, **91**, 053503–053506.

19. J. L. Blackburn, D. C. Selmarten, and A. J. Nozik, *J. Phys. Chem. B*, 2003, **107**, 14154–14157.

20. T. Zewdu, J. N. Clifford, J. P. Hernández, and E. Palomares, *Energy Environ. Sci.*, 2011, **4**, 4633–4638.

21. Y. Tachibana, K. Umekita, Y. Otsuka, and K. Susumu, *J. Phys. Chem. C*, 2009, **113**, 6852–6858.

22. H. Lee, H. C. Leventis, S.-J. Moon, P. Chen, S. Ito, S. A. Haque, T. Torres, F. Nüesch, T. Geiger, S. M. Zakeeruddin, M. Grätzel, and M. K. Nazeeruddin, *Adv. Funct. Mater.*, 2009, **19**, 2735–2742.

23. D. R. Baker and P. V. Kamat, *Adv. Funct. Mater.*, 2009, **19**, 805–811.

24. N. Guijarro and T. Lana-Villarreal, *J. Phys. Chem. C*, 2010, 21928–21937.

25. P. Kambhampati, *Acc. Chem. Res.*, 2011, **44**, 1–13.

26. P. Kambhampati, *J. Phys. Chem. C*, 2011, **115**, 22089–22109.

27. M. Achermann, M. A. Petruska, S. A. Crooker, and V. I. Klimov, *J. Phys. Chem. B*, 2003, **107**, 13782–13787.

28. V. I. Klimov, *J. Phys. Chem. B*, 2000, **104**, 6112–6123.

29. B. T. Spann, L. Chen, X. Ruan, and X. Xu, *Opt. Express*, 2013, **21**, A15–A22.

30. B. T. Spann and X. Xu, *J. Phys. Chem. C*, 2014, **118**, 2844–2850.

31. J. Sambur, T. Novet, and B. Parkinson, *Science (80-.).*, 2010, **330**, 63–66.

32. Y. Yang, W. Rodríguez-Córdoba, X. Xiang, and T. Lian, *Nano Lett.*, 2012, **12**, 303–309.

33. J. Pijpers, R. Koole, W. H. Evers, A. J. Houtepen, S. Boehme, C. de M. Donega, D. Vanmaekelbergh, and M. Bonn, *J. Phys. Chem. C*, 2010, **114**, 18866–18873.

34. E. Cánovas, P. Moll, S. A. Jensen, Y. Gao, A. J. Houtepen, L. D. A. Siebbeles, S. Kinge, and M. Bonn, *Nano Lett.*, 2011, **11**, 5234–5239.

35. K. Zheng, K. Z□ídek, M. Abdellah, P. Chábera, M. S. Abd El-sadek, and T. Pullerits, *Appl. Phys. Lett.*, 2013, **102**, 163119 (1–5).

36. D. A. H. Hanaor and C. C. Sorrell, *J. Mater. Sci.*, 2010, **46**, 855–874.

37. J. Li, M. W. G. Hoffmann, H. Shen, C. Fabrega, J. D. Prades, T. Andreu, F. Hernandez-Ramirez, and S. Mathur, *J. Mater. Chem.*, 2012, **22**, 20472–20476.

38. S. P. S. Porto, P. A. Fleury, and T. C. Damen, *Phys. Rev.*, 1967, **154**, 522–526.

39. K. Tvrdy and P. V Kamat, *J. Phys. Chem. A*, 2009, **113**, 3765–3772.

40. V. I. Klimov, *Annu. Rev. Phys. Chem.*, 2007, **58**, 635–73.

41. L. A. Padilha, J. T. Stewart, R. L. Sandberg, W. K. Bae, W.-K. Koh, J. M. Pietryga, and V. I. Klimov, *Acc. Chem. Res.*, 2013, **46**, 1261–9.

42. J. L. Blackburn, D. C. Selmarten, R. J. Ellingson, M. Jones, O. Micic, and A. J. Nozik, *J. Phys. Chem. B*, 2005, **109**, 2625–31.

43. I. Robel, B. A. Bunker, and P. V. Kamat, *Adv. Mater.*, 2005, **17**, 2458–2463.

44. D. Tsukamoto, Y. Shiraishi, Y. Sugano, S. Ichikawa, S. Tanaka, and T. Hirai, *J. Am. Chem. Soc.*, 2012, **134**, 6309–6315.

45. K. Žídek, K. Zheng, C. S. Ponseca, M. E. Messing, L. R. Wallenberg, P. Chábera, M. Abdellah, V. Sundström, and T. Pullerits, *J. Am. Chem. Soc.*, 2012, **134**, 12110–12117.

46. R. Asahi, Y. Taga, W. Mannstadt, and A. J. Freeman, *Phys. Rev. B*, 2000, **61**, 7459–7465.

47. C. G. Van de Walle and J. Neugebauer, *Nature*, 2003, **423**, 626–628.

48. Y. Yang, Z. Liu, and T. Lian, *Nano Lett.*, 2013, **13**, 3678–3683.

49. Y. Gao, E. Talgorn, M. Aerts, M. T. Trinh, J. M. Schins, A. J. Houtepen, and L. D. A. Siebbeles, *Nano Lett.*, 2011, **11**, 5471–5476.

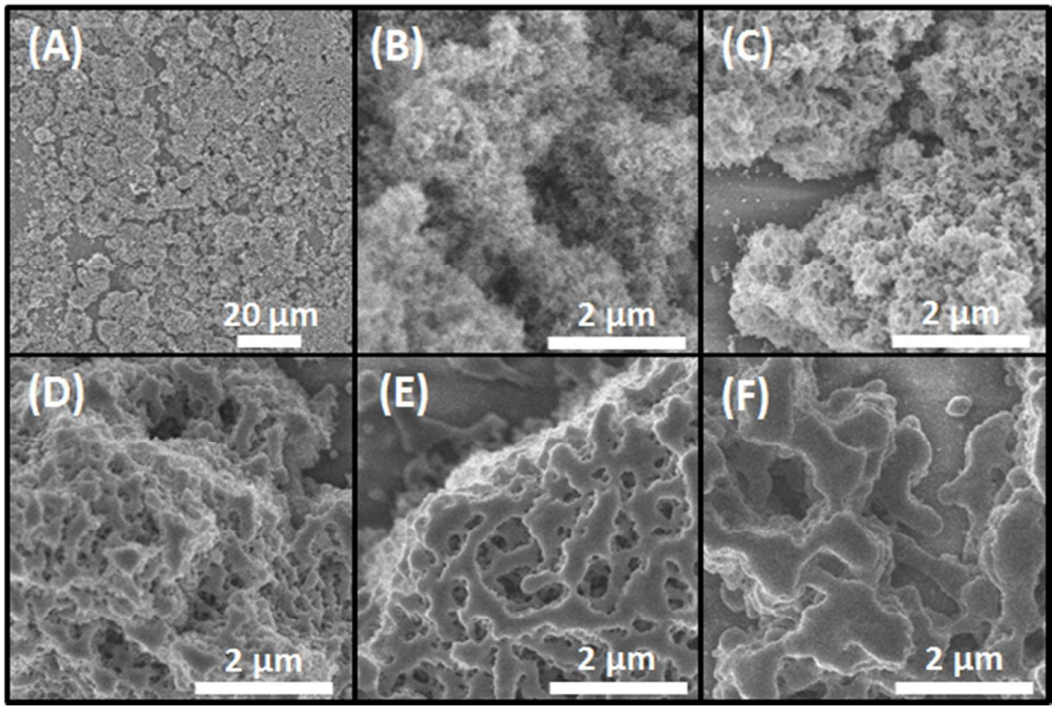

Figure 1. Surface SEM images of the TiO_2 NC films prior to CdS adsorption. (A) is a representative image of a 50 µm scaled image of the un-sintered film, (B) is of an un-sintered film, with as prepared TiO_2 nanocrystals (~ 10 nm diameter), (C), (D), (E), and (F) are films sintered using laser fluences of 50, 100, 150, and 200 mJ/cm^2, respectively.

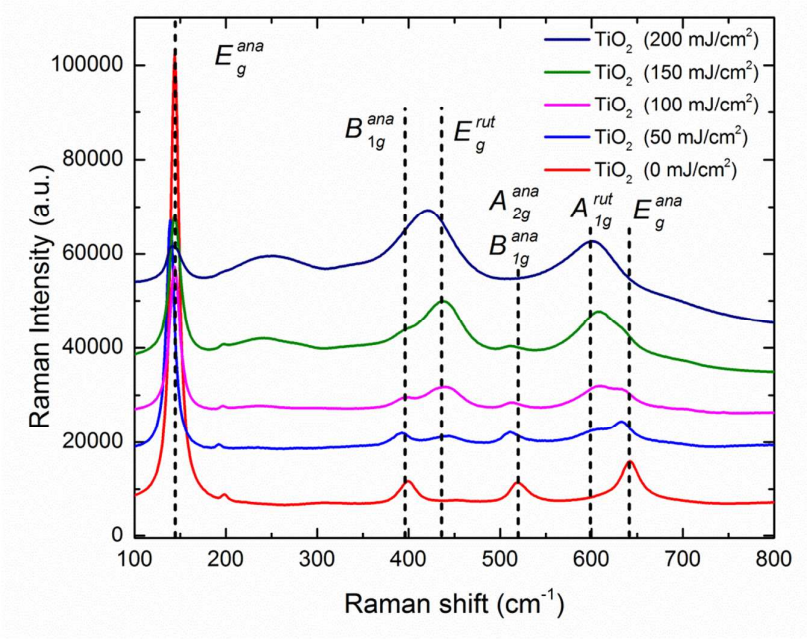

Figure 2. Raman spectra of un-sintered (0 mJ/cm^2) and sintered TiO_2 samples using laser fluence of 50, 100, 150, and 200 mJ/cm^2. The dashed vertical lines denote pure phase Raman shift peaks, superscripts (ana) and (rut) reflect anatase and rutile phases, respectively.

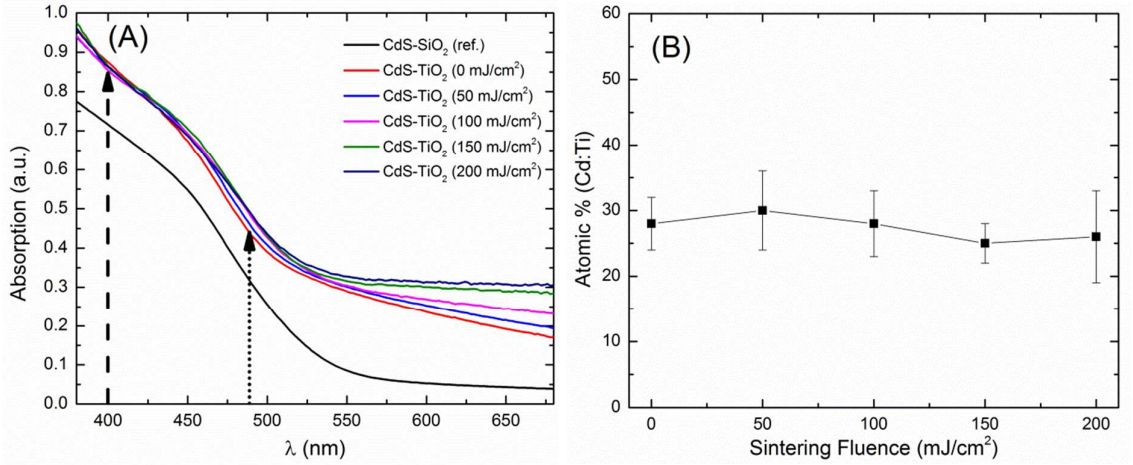

Figure 3. (A) Linear absorption spectra of CdS–SiO_2 (reference sample) and CdS–TiO_2 samples with various TiO_2 sintering conditions. Also shown are pump (dashed arrow) and probe (dotted arrow) wavelengths for the transient absorption measurements. (B) Relative amount of Cd to Ti for the samples; ratios were obtained from EDX data.

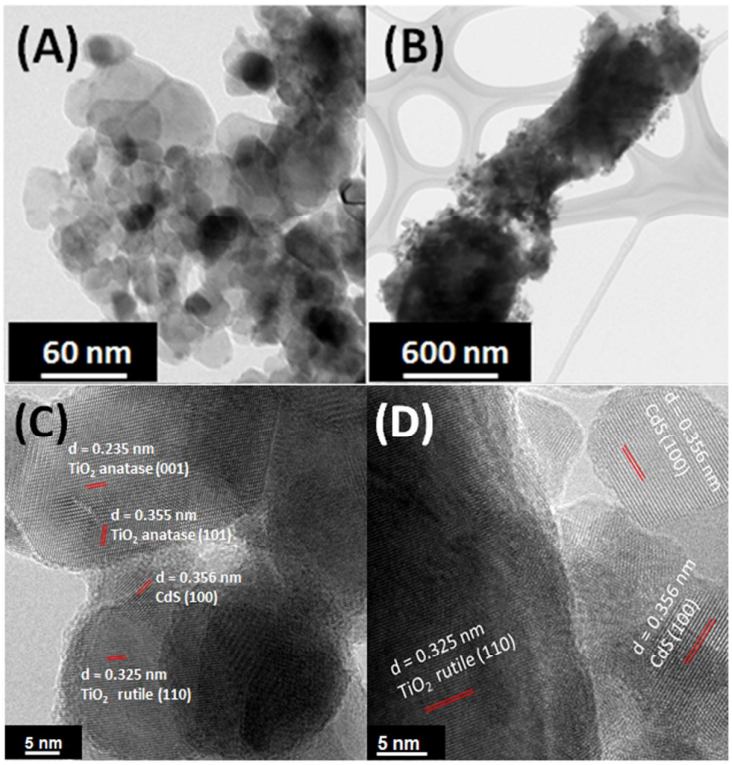

Figure 4. Low resolution TEM images of CdS adsorbed to TiO_2, (A) before sintering, (B) after sintering showing the change in morphology of TiO_2 particles. High resolution TEM images (C) before sintering, and (D) after sintering with the crystal planes marked for rutile and anatase TiO_2 indicating the phase transformation; the adsorbed CdS are also marked, for clarity and to reveal the interface between CdS and TiO_2.

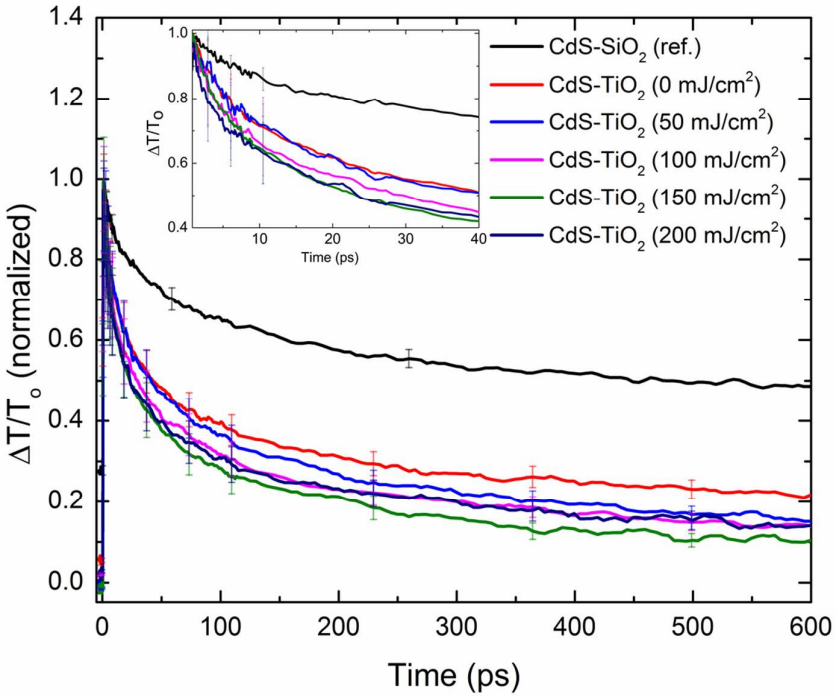

Figure 5. Transient absorption spectroscopy data of CdS–SiO_2 (reference sample) and CdS–TiO_2 samples for all sintering conditions. Note the CdS–SiO_2 is an un-sintered sample. The data represent the average of five spatial locations on the sample with the error bars representing one standard deviation between the various spatial locations. The inset shows the first 40 ps.

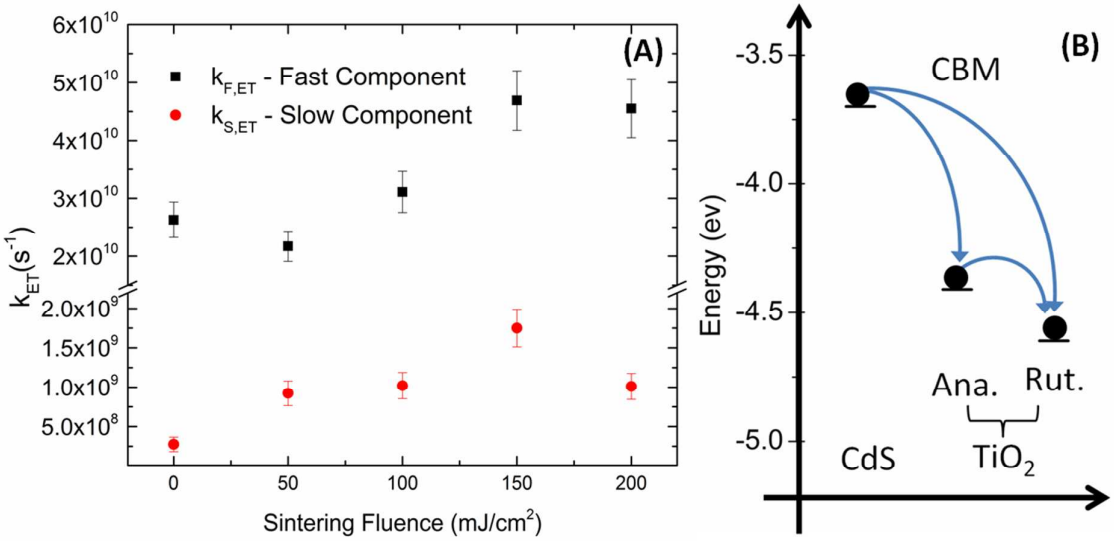

Figure 6. (A) Fast and slow components of calculated electron transfer rates (k_{ET}) from the adsorbed CdS nanocrystals to TiO_2. (B) Shows charge transfer pathways on a vacuum energy level diagram, *e.g.*, the band-edge electron in the CdS nanocrystal can transfer to anatase (Ana.) or to rutile (Rut.) phase TiO_2 or sequentially transfer from CdS to anatase then to rutile TiO_2.

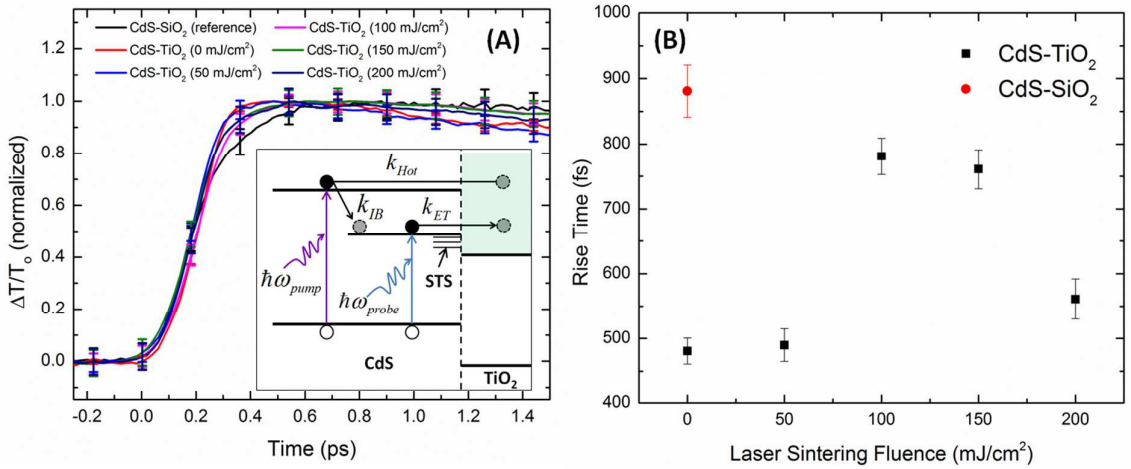

Figure 7. Normalized early rise timetransient absorption signals with background photoluminescence subtracted from the CdS-SiO_2 sample for direct comparison, and corresponding rise time values as a function of sintering fluences shown in (A) and (B), respectively. Inset of (A) shows potential early-time relaxation pathways, including hot electron transfer (k_{Hot}), intraband relaxation rate (k_{IB}), and cold/band-edge electron transfer (k_{ET}).

Table 1: Biexponential Fitting and Charge Transfer Rate Results from Transient Absorption Data

	Sintering Fluence (mJ/cm^2)	C_1	$\tau_1(s)$	C_2	$\tau_2(s)$	$k_{F,ET}(s^{-1})$	$k_{S,ET}(s^{-1})$	$\langle k_{ET} \rangle (s^{-1})$
CdS-SiO_2*	N.A.	0.28	2.76E-11	0.72	8.13E-10	N.A.	N.A.	N.A.
CdS-TiO_2	0	0.47	1.60E-11	0.53	6.64E-10	2.63E+10	2.76E+08	2.91E+08
	50	0.48	1.72E-11	0.52	4.65E-10	2.17E+10	9.22E+08	9.77E+08
	100	0.52	1.48E-11	0.48	4.44E-10	3.11E+10	1.02E+09	1.08E+09
	150	0.56	1.20E-11	0.44	3.35E-10	4.69E+10	1.75E+09	1.86E+09
	200	0.53	1.22E-11	0.47	4.47E-10	4.55E+10	1.01E+09	1.06E+09

*The background PL signal has been subtracted and the signal is re-normalized and fitted for the charge transfer calculations.

Table of Contents Graphic

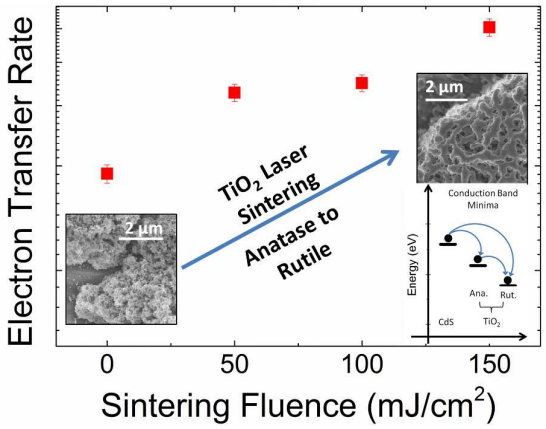

We show a means of increasing charge transfer in CdS–TiO_2 heterojunctions by laser sintering TiO_2 nanocrystals.